



Chloride gradient render carrier extraction of hole transport layer for high V_{oc} and efficient inverted organometal halide perovskite solar cell

Kai-Chi Hsiao^{a,b}, Bo-Ting Lee^a, Meng-Huan Jao^a, Ting-Han Lin^c, Cheng-Hung Hou^{a,d},
Jing-Jong Shyue^{a,d}, Ming-Chung Wu^{c,e,f}, Wei-Fang Su^{a,b,*}

^a Department of Materials Science and Engineering, National Taiwan University, Taipei City 10617, Taiwan

^b Advanced Research Center for Green Materials Science and Technology, National Taiwan University, Taipei City 10617, Taiwan

^c Department of Chemical and Materials Engineering, Chang Gung University, Taoyuan City 33302, Taiwan

^d Research Center for Applied Sciences, Academia Sinica, Taipei 11529, Taiwan

^e Green Technology Research Center, Chang Gung University, Taoyuan City 33302, Taiwan

^f Division of Neonatology, Department of Pediatrics, Chang Gung Memorial Hospital, Taoyuan City, 33305, Taiwan

ARTICLE INFO

Keywords:

Chloride gradient
Nickel oxide
Passivation
Hole transport material
Perovskite
Solar cell

ABSTRACT

A carrier transport layer and its interfacial effects on an organometal halide perovskite light harvesting layer play an influential factor in either photovoltaic performance or long-term stability of a perovskite solar cell (OHPSC). Although the understandings of the carrier transport layers and interfacial effects on regular structured OHPSCs have been explored, knowledge of an interface between hole transport layer of NiO_x and perovskite in an inverted OHPSC is still necessary to be developed. Here, we performed a universal NiO_x film with the sequential passivation strategy of NiCl_2 (SPS- NiCl_2 treatment) for either wide bandgap or narrow bandgap of OHPSCs. The SPS- NiCl_2 treated NiO_x film not only implements the passivation at the perovskite layer/ NiO_x film interface but also confers itself a gradient energy level of valance band inducing by chloride. Comprehensive characterizations reveal that the SPS- NiCl_2 treated NiO_x film suppresses non-radiative recombination at the interface and enlarges the splitting of the quasi-Fermi level at the interfaces. The photoconversion efficiency (PCE) of the champion device comprised of the SPS- NiCl_2 treated NiO_x film can achieve 19.53% with a record V_{oc} of 1.16 V, the lowest V_{oc} deficit of 390 mV in NiO_x based inverted OHPSCs. The corresponding devices with encapsulation also exhibit superior long-term stability, and over 80% of initial PCE can be maintained after 1500 h damp-heat test. This study sheds the light on managing the interfacial issues of an inverted OHPSC and offers a feasible path to develop a universal hole transport layer for perovskite layers with different energy bandgap.

1. Introduction

Organometal halide perovskite materials (OHPVSKs) have attracted lots of attention and have become one of the most potential photovoltaic materials owing to their remarkable optoelectronic properties. The unique band structure of OHPVSK confers it to have a high absorption coefficient [1], long diffusion length [2,3], and high carrier mobility [4]. Applications of lighting and energy harvesting based on OHPVSKs have led to a revolutionary surge in photovoltaic society. The unprecedented progress of power conversion efficiency achieves from 3.9% to over 25% in a short span of the development of organometal halide perovskite solar cells (OHPSCs) [5]. Generally, the classic architecture of OHPSCs can be categorized into two types: regular structure of n-i-p mesoporous

and planar structure; inverted structure of p-i-n planar structure. Among them, inverted planar structure catches a lot of attention because of its large process window and much reliable photoconversion efficiency (PCE) with negligible hysteresis.

An ideal hole transport layer (HTL) for high efficient inverted device has to meet the criteria such as (i) high optical transmittance [6], (ii) large energy band gap, (iii) corresponding deep energy level of valance band maximum (VBM) [7,8], (iv) good extraction ability for excited hole [9], and (v) uniform morphology for crystallization of perovskite film. According to the materials of HTL for OHPSCs, they can be categorized into triarylamine-based molecules, polymer, and metal oxide-based inorganic compounds. Although a high efficiency of OHPSC can be obtained with an organic HTL because of its suitable energy alignment as

* Corresponding author at: Department of Materials Science and Engineering, National Taiwan University, Taipei City 10617, Taiwan.

E-mail address: suwf@ntu.edu.tw (W.-F. Su).

<https://doi.org/10.1016/j.cej.2020.128100>

Received 21 October 2020; Received in revised form 2 December 2020; Accepted 9 December 2020

Available online 14 December 2020

1385-8947/© 2020 Elsevier B.V. All rights reserved.

well as carrier mobility, the inferior thermal or chemical stability compared to metal-oxide based inorganic compounds impede their development and application.

From material point of view to improve stability and to prolong the lifetime of OHPSCs, a chemical and physical stable metal-oxide based p-type semiconductor is of a more appropriate choice than organic-based molecules and polymers. Nickel oxide (NiO_x) holds several advantages over the other counterparts because of its chemical stability, large energy bandgap (E_g), deep energy level of VBM. When acting as a hole transporting material, conductivity and interface effect of NiO_x that includes surface morphology, energy level alignment, and interfacial defects are of the overarching factors to obtain an efficient OHPSC. The self-doping effect of Ni^{3+} in a NiO_x film has been reported to be a feasible methodology to enhance the conductivity [10–12]. Therefore, many strategies such as monovalent/trivalent cation doping; interstitial oxygen and/or nickel vacancy point defect creation were adopted to increase the ratio of Ni^{3+} in a NiO_x film [13–17]. Although a precise controlling of dopant in a NiO_x film promotes its conductivity, the hole extraction ability of an HTL is highly dependent on interfacial interaction between adjacent layers.

Defects at interface and energy alignment between adjacent layers are the main issue as discussing the interfacial effects [18,19]. Interfacial defects play the role of carrier scavengers and annihilate transporting carriers via non-radiative recombination [20,21]. Reduction of interfacial defects as well as interfacial recombination velocities are always sought in photovoltaics to approach high quantum efficiency and operating efficiency closing to radiative limitation [22–24]. On the other hand, the selective contact layers, here are electron transport layer (ETL) and HTL, in an OHPSC create built-in potential (V_{bi}) and quasi-Fermi levels at the interfaces as they contact to each other. The splitting of the quasi-Fermi levels at interfaces is proportional to open-circuit voltage (V_{oc}) of an OHPSC. That is, the interfacial effects influences on ability of carrier collection of a selective contact layer and further on a value of V_{oc} as assembling a complete OHPSC. Moreover, quick transporting of hot carriers is another method to extract carriers and further harvest photogenerated current [25]. To achieve high photovoltaic performance, passivation strategies have been proposed to diminish the interfacial defects and to improve the energy alignment between adjacent layers. For instance, chlorine atoms at the interface between an ETL and perovskite layer were reported to suppress the deep trap state and to compensate for the dangling bond at the surface of the perovskite layer [26]. A presence of a hydrophobic molecule at interfaces can modify the surface tension of a perovskite precursor and tailor the nucleation process of its layer growth [27–29]. Also, inducing a gradient dopant in charge transport layers was reported to create a continuous change of energy level in the transport layers. That helps the charge transport layers collect hot carrier with less non-radiative recombination than that without continuous energy level [30,31]. Although the understanding of the interfacial effects on photovoltaic performance of regular OHPSCs was explored [32–35], there is still lack of technique to simultaneously manage interfacial effects and energy alignment, especially for inverted OHPSCs [36–38]. In aim to deal with the interfacial effects aforementioned, establishing a NiO_x film exhibiting a low defect density and continuous energy level of VBM is urgently needed to resolve the issues.

Here in this study, a universal NiO_x hole transporting layer exhibiting a continuous change of VBM was demonstrated via a sequential passivation strategy with NiCl_2 (SPS- NiCl_2 treatment). The SPS- NiCl_2 treated NiO_x films take advantage of exhibiting a high ratio of Ni^{3+} at surface, low defect densities, and a VBM gradient in depth. The VBM gradient induced from chloride (Cl^-) and high ratio of Ni^{3+} at NiO_x film provides an effective pathway for hole transportation for either narrow E_g or wide E_g perovskite layers. The Cl^- gradient effects on energy level alignment and electrical properties are comprehensively investigated through ultraviolet photoelectron spectrometer (UPS) and depth profile of X-ray photon spectrometer (XPS). The charge carrier transport/recombination dynamics of perovskite films and OHPSCs based on such

an HTL were explored by using time-resolved photoluminescence spectrum (TR-PL) and driven-level capacitance profiling (DLCP). The results show that Cl^- gradient can shift the VBM of NiO_x film downward and increase the ratio of Ni^{3+} at surface of NiO_x film. Meanwhile, the film coverage of NiO_x film increased from 91.15% to 97.05% with improved surface morphology. The highest coverage and appropriate energy gradient of the SPS- NiCl_2 treated NiO_x film enhanced the power conversion efficiency of OHPSC from 18.16% to 19.53% with the V_{oc} of 1.16 V, which is the highest for NiO_x based inverted OHPSCs. As applying to the wide bandgap OHPSCs, the V_{oc} of such devices can also be boosted to 1.17 V for perovskite with $E_g = 1.65$ eV and 1.23 V for perovskite with $E_g = 1.70$ eV. The encapsulated devices with such HTL can still deliver over 80% of their initial PCE after 1500 h of damp-heat test (85 RH% and 85 °C). These results reveal that the SPS- NiCl_2 treatment simultaneously improves energy alignment, electrical property, and surface morphology of NiO_x films. That can be directly implemented on OHPSCs with different E_g of perovskite layers and results in superior photovoltaic performance and long-term stability of the corresponding devices.

2. Experimental section

2.1. Material and method

Here the chemicals in this study such as methylammonium iodide (99%, FMPV®), methylammonium bromide (98%+, FMPV®), formamidinium iodide (98%+, FMPV®), cesium iodide (99.9%, Alfa Aesar), lead iodide (99.9985%, Alfa Aesar), lead bromide (99.9985%, Alfa Aesar), 6,6-phenyl-C61-butyric acid methyl ester (PC₆₁BM, 99%, FMPV®), polyethylenimine (branched PEI, 80%, Sigma-Aldrich), nickel acetate tetrahydrate (98%, Kanto® Chemicals), nickel chloride hexahydrate (99%, Sigma-Aldrich), gamma butyrolactone (99%, ACROS Organics), dimethyl sulfoxide (99.7%, ACROS Organics), anhydrous ethanol (99.5%, Sigma-Aldrich), ethanolamine (98%+, Sigma-Aldrich), isopropanol (99.5%, ACROS Organics), and chlorobenzene (99%, ACROS Organics) were used without any purification process.

For dipolar ion passivation of thiophene ethyl ammonium chloride (TEACl), TEACl was synthesized following by the previous study [39]. Briefly, equal stoichiometry precursors of 2-(aminomethyl)thiophene (98%, Tokyo Chemical Industry Co., Ltd.) and hydrochloric acid (36.5–38.0%, Sigma-Aldrich) were mixed and stirred in an ice bath for 2 h. The excess solvent in the resultant solution was thereafter removed by using a rotary evaporator. The bright yellow powder of the product was collected in a vial bottle and washed with the non-polar solvent of diethyl ether (99%, Fisher) three times. The color of the powder faded from mild yellow to transparent white. A recrystallization method was then carried out to further purify the reactant. Finally, the transparent white reactant of TEACl was placed in a vacuum condition for 12 h and then stored in N_2 atmosphere.

2.2. Solution preparation and device fabrication

All the solution preparation and device fabrication were followed by the previous study [39,40]. For hole transporting layer of the pristine NiO_x layer, a half mmole of nickel acetate tetrahydrate was dissolved in 1 mL of ethanol with 30 μL of ethanolamine. For the precursor solution of the SPS- NiCl_2 treatment, different concentrations of 0.125, 0.250, and 0.500 mmol of nickel chloride hexahydrate were dissolved into 1 mL of ethanol. The active layer of narrow bandgap perovskite, an equal mole of MAI and PbI_2 were mixed and dissolved into a co-solvent system of DMSO and GBL with a volume ratio of 3/7 to obtain a precursor solution with a concentration of 0.6 M. On the other hand, for wide bandgap perovskite layer, the same concentration and co-solvent system as narrow bandgap perovskite were used to prepare the precursors. To avoid the bromide phase segregation, the bromide ratio of 20% was fixed to prepare either CsFA based or CsMA based wide bandgap perovskite

precursor solutions. For CsFA based perovskite ($E_g = 1.65$ eV), the solutes of 0.12 mmole CsI, 0.36 mmole FAI, 0.12 mmole FABr, 0.48 mmole PbI_2 , and 0.12 mmole of $PbBr_2$ were mixed and dissolved into the DMSO/GBL co-solvent system. Whereas the CsMA based perovskite ($E_g = 1.70$ eV), the solutes including 0.06 mmole of CsI, 0.12 mmole of MABr, 0.42 mmole of MAI, 0.48 mmole of PbI_2 , and 0.12 mmole of $PbBr_2$ were dissolved into the same co-solvent system. Prior to use, all the perovskite precursors should be stirred at 70 °C overnight to ensure the complete dissolving of the solutes. For an electron transporting layer and a work function modified layer, 20 wt% of $PC_{61}BM$ and 0.1 wt% of PEI were obtained by dissolving them in chlorobenzene and isopropanol, respectively.

The procedure of a p-i-n hot casting perovskite device was followed by the previous study [39–41]. A hole transporting layer of either pristine NiO_x or the SPS- $NiCl_2$ treated NiO_x film was deposited onto an FTO glass (8 Ω /sq, STAREK®) by a spin-coating process. For a pristine NiO_x film, the as-prepared precursor was spin-coated at a spin rate of 4000 rpm and followed with a calcined step at 300 °C for 30 min. On the other hand, the SPS- $NiCl_2$ treated NiO_x films were processed with two steps at a higher spin rate of 6000 rpm. Prior to the SPS- $NiCl_2$ treatment, a layer of pristine NiO_x was first deposited and calcined at 300 °C for 10 min. Secondly, the SPS- $NiCl_2$ was post-treated on the as-prepared NiO_x film and calcined at 300 °C for 20 min. To control the thickness of the SPS- $NiCl_2$ treated NiO_x films to be the same as the control NiO_x films (the thickness of HTLs are 90 nm \pm 10 nm), the spin rate of the SPS- $NiCl_2$ treatment was increased from the original 4000 rpm to 6000 rpm. Prior to perovskite film deposition, the as-prepared substrates (FTO/ NiO_x or the SPS- $NiCl_2$ treated NiO_x) were placed at a pre-heated hot plate. The pre-heated temperature depends on the type of perovskite precursors. For narrow bandgap and CsMA based wide bandgap perovskite, the corresponding temperature was 150 °C, whereas the CsFA based wide bandgap perovskite was 180 °C. Additionally, to increase the wettability of precursor solutions, all precursors were pre-heated at 75 °C. The pre-heated steps maintain for 10 min to achieve thermal equilibrium. All the perovskite layers were fabricated in humidity-controlled air (RH% < 10%) via hot-casted deposition. The typical procedure was carried out by spin coating at 4000 rpm for 15 s immediately as the perovskite precursor solution dripped onto a hot substrate. In order to compensate for the defects at perovskite/ETL interface, the passivation of TEACl was carried out to enhance the photovoltaic performance [39]. Subsequently, the ETL of $PC_{61}BM$ was spin-coated onto the perovskite layers. Prior to deposit a silver (Ag) electrode, a work function modifier of polyethylenimine (PEI) was spin-coated onto the ETL. Eventually, Ag electrodes with 100-nm thickness were deposited using thermal evaporation with an active area of 0.09 cm². To evaluate the device performances, the results were all summarized from 48 devices from 8 different batches. Each batch consisted of 6 devices and therefore the statistical data points in this study are summarized by 48 devices. For dynamic carrier recombination, time-resolved photoluminescence (TR-PL) was employed to analyze carrier lifetime of samples. The perovskite films were directly deposited onto glass substrates or glass with HTLs based on the aforementioned protocol. In terms of devices with encapsulation, an FTO glass was first patterned by laser scribe with wavelength of 532 nm. The same structure of device was deposited onto the patterned FTO glass. A UV curable epoxy resin was utilized to fully cover the device. A coverslip thereafter capped onto the device and the curing process was carried out with a UV-A lamp ($\lambda = 365$ nm). Finally, a butyl rubber paste was thermal-pressed at the edges of the coverslip to prevent permeation from the gap between the epoxy layer and the coverslip.

2.3. Characterization of material and devices

The solar simulator source (YAMASHITA DENSO, YSS-200A, class AAA) equipped with a 1600-W Xenon short-arc lamp was used to analyze the photovoltaic performance of devices. The photocurrent density (I)-voltage (V) curve of solar cell devices were all measured in air

under A.M. 1.5 irradiation (100 mW/cm²) and recorded by the Keithley 2410 source meter. Prior to the measurements, the light intensity of the solar simulator was calibrated by using a KG-5 filtered mono-crystalline silicon standard cell to adjust miss-matched spectra and to obtain the unity of measurements. The I - V characteristics of devices were analyzed from both forward (-0.2 to 1.2 V) and backward (1.2 to -0.2 V) scans. For driven-level capacitance profiling (DLCP), an 10 mV of alternating current with 1, 10, 100, 500, and 1000 kHz frequency was applied to a complete device for measurement. For the XPS and depth profile of XPS, all spectra were acquired by a PHI 5000 VersaProbe (ULVAC-PHI, Japan) system. For XPS depth profiling, a monochromatic Al K α X-ray with a beam diameter of 100 μ m was applied to generate the characteristic photoelectrons. During data acquisition, the investigated surface was neutralized by an electron and an Ar⁺ ion beam. In order to remove the surface material, a 1 kV-Ar⁺ ion beam with a beam current of 735 nA was utilized as the etching source. For UPS measurements, He I line (21.2 eV) generated by a discharge lamp was used as the light source. All the UPS spectra were acquired with a stage bias of -7 V and a thermally evaporated Au film was used as a reference to determine the Fermi level. Therefore, the work function of materials can be identified by subtracting vacuum level (21.2 eV) with energy cutoff (E_{cutoff}). In addition, the energy difference between Fermi level and valance band maximum of materials is also determined at the origin and offset point. For carrier behavior analyses, a 440-nm continuous-wave diode laser (DONGWOO, PDLH-440-25) was applied to excite the perovskite films to quantify steady-state photoluminescence (PL), continuous PL, and time-resolved PL (TRPL). The TR-PL spectra were examined by using a pulse laser with an average power of 1 mW and were recorded by a time-correlated single-photon counting (TCSPC) (WELLS-001 FX, DONGWOO OPTRON) spectrometer at a frequency of 312.5 MHz and delay span of 2 μ s. Micrographs of perovskite films were all acquired by an FE-SEM (Hitachi, SU8000, 15-kV voltage, 10.0 mm working distance). The energy-dispersive X-ray spectroscopy (EDS) (Xflash Detector 5030, Bruker) and cross-sectional images were all acquired from the FE-SEM. The Grazing-Incidence Wide-Angle X-ray Scattering (GIWAXS) spectra of samples were obtained using synchrotron X-ray source ($\lambda = 1.00575$ Å) at BL13A1 scattering end station of the National Synchrotron Radiation Research Center (NSRRC) in Hsinchu, Taiwan. The NiO_x films were deposited on 2 \times 2 cm² silicon wafers by following the same protocol as the photovoltaic devices. In order to avoid the severe interaction between incident X-ray and characterized samples. The angles of incident X-ray was manipulated at the range from 1 to 2°. The information of scattering thereafter was collected by a two-dimensional detector. For long-term stability testing, the encapsulated devices were placed into a constant humidity (85% RH) and temperature (85 °C) chamber (Terchy, HRMB-80) for damp-heat testing.

3. Results and discussion

The NiO_x films with and without sequential passivation strategy $NiCl_2$ (SPS- $NiCl_2$) were prepared from sol-gel method. Briefly, a pristine NiO_x film was obtained from spin-coated deposition of 0.500 M nickel acetate precursor solution on an FTO glass and followed by a calcination step at 300 °C for 30 min. For NiO_x films with the SPS- $NiCl_2$ treatment, different concentrations of $NiCl_2$ precursors (0.125 M, 0.250 M, and 0.500 M) were thereafter applied for post treatment onto crystallized NiO_x films and calcinated with the same process respectively (details see in experimental section). The sample names of such treatment were denoted as SPS- $NiCl_2$ -0.125, SPS- $NiCl_2$ -0.250, and SPS- $NiCl_2$ -0.500 in the following discussion. The thickness of each HTL were monitored at 90 nm \pm 10% and shown in Fig. S1. Owing to the calcination process for crystallization of NiO_x films, microcracks induced by shrinkage easily appears as the NiO_x films solidify from a precursor state into a crystallized thin film. As an optimal HTL for inverted OHPSCs, the compacted morphology in macroscopic point of view and energy alignment between adjacent layers in microscopic point of view are the overarching

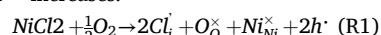
factors. Such microcracks in HTL give an opportunity for the contact of the bottom anode and the perovskite film and therefore cause leakage of current as OHPSC under operation [42]. Fig. 1 shows the completely microscopic observations involving in nanomorphology of field-emission scanning electron microscope (FE-SEM, the first row) and topography of atomic force microscope (AFM, the second row) of the NiO_x film and NiO_x films with different concentrations of the SPS-NiCl₂ treatment. From images obtained by FE-SEM (first row of Fig. 1), the coverage percentage of NiO_x film was culminated to 97.05% as the concentration of the SPS-NiCl₂ solution increased to 0.250 M. The NiCl₂ precursor infiltrated and further fulfilled the microcracks in NiO_x films after the SPS-NiCl₂ treatment. However, the high concentration of the SPS-NiCl₂ treatment resulted in an inevitable aggregation at top of a NiO_x film and leading to a poor film formation of the SPS-NiCl₂ treatment. Thus, the average roughness (R_a) of SPS-NiCl₂-0.500 deteriorated from 13.4 nm to 15.9 nm as shown in topography from AFM images (second row of Fig. 1). The coverage also decreases from 97.05% to 94.75% owing to the aggregation induced by the concentrated SPS-NiCl₂ treatment of 0.500 M. To investigate whether FTO were covered, Fig. S2 shows the EDS analysis of NiO_x films without or with the SPS-NiCl₂ treatment. Based on the atomic ratio analysis of tin in Table S1, the SPS-NiCl₂ treatment can not only improve the surface roughness of NiO_x films but also ensure the fully coverage of FTO layer even at crack sites induced by poor film formation of too high concentration treatment. Such SPS-NiCl₂ treated NiO_x films prevent devices from shunting of direct contacting between FTO and perovskite layer.

In addition to the surface morphology, increasing the concentration of Ni³⁺ in a NiO_x film can rationally infer to enhance the conductivity through the self-doping effect. The SPS treatment from NiCl₂ precursor is speculated to modify the oxidation state of nickel owing to the presence of a monovalent anion of chloride. The chloride is speculated to stabilize the presence of Ni³⁺. The strong electron affinity of chloride offers the preference of Ni³⁺ formation compared to the condition of Ni-O bonding. Fig. 2 shows the Ni 2p orbital of NiO_x films with and without the SPS-NiCl₂ treatment.

The peak of Ni³⁺ and Ni²⁺ shows obvious variations as NiO_x film with the SPS-NiCl₂ treatment. To investigate the influences of chloride on Ni oxidation state, the atomic ratios of Ni³⁺/Ni, O/Ni, and Cl/O were

calculated from the peak ratios of the corresponding X-ray photoelectron spectrum (XPS) in Figs. 2 and S3. The results were summarized in Table 1. The ratio of Ni³⁺/Ni increases from 57.98 at. % to above 64.00 at. % when NiO_x films were post-treated with SPS-NiCl₂ solution. During the SPS-NiCl₂ treatment, the byproduct of hydrochloride acid was released. As a strong Lewis acid, hydrochloride acid easily protonated the alcohol or water in the solution of NiCl₂ and form an electron deficient species of C₂H₅O⁺H₂ or H₃O⁺ and Cl⁻. The protonated species in the NiCl₂ film facilitate the oxidation of Ni²⁺ during the formation and crystallizing step of NiO_x film and result in the presence of Ni³⁺ [13]. Since Ni²⁺ is energetically favorable compared to Ni³⁺ [43], the electron-rich Cl⁻ is speculated to play a role of stabilizing the Ni³⁺. Therefore, the increase content of Ni³⁺ can be attributed to the present of Cl⁻ [44]. The atomic ratio of O/Ni again shows an obvious increase as NiO_x films applied the SPS-NiCl₂ treatment. As a volatile product of chloride, the atomic ratio of Cl/O is remained at around 3 at. % even though treating NiO_x films with higher concentration of the SPS-NiCl₂ solution. The excess chloride degases from the NiO_x film and the concentration of chloride remains at about 3 at. % after the calcination. Therefore, the Ni³⁺/Ni ratio slightly increases even increasing the concentration of the SPS-NiCl₂ solution to 0.500 M. Moreover, the severe aggregation occurs when the concentration of SPS-NiCl₂ solution is too high to form a uniform film during the treatment as shown in AFM images (Fig. 1).

The self-dopant of Ni³⁺ is thought of as the spices rendering the conductivity of NiO_x films. [11,45,46] The hypothesis of NiO_x film with the SPS-NiCl₂ treatment is expressed as reaction (R1). The Ni³⁺ ions are speculated to be stabilized when chloride ions occupy the interstitial site. Therefore, the conductivity of NiO_x films increases as the content of Ni³⁺ increases.



To validate the above hypothesis, the Hall effect of NiO_x films and films with the SPS-NiCl₂ treatment was characterized and summarized in Table 2. The conductivity of a material is composed of density and mobility of charge carrier. From Hall effect characterization, the carrier density of NiO_x film enhances three times with 0.250 M of the SPS-NiCl₂ treatment. Also, the mobility increases from 0.90 cm² V⁻¹ s⁻¹ to 27.90 cm² V⁻¹ s⁻¹. Based on Scherrer equation, the grain size of NiO_x films can

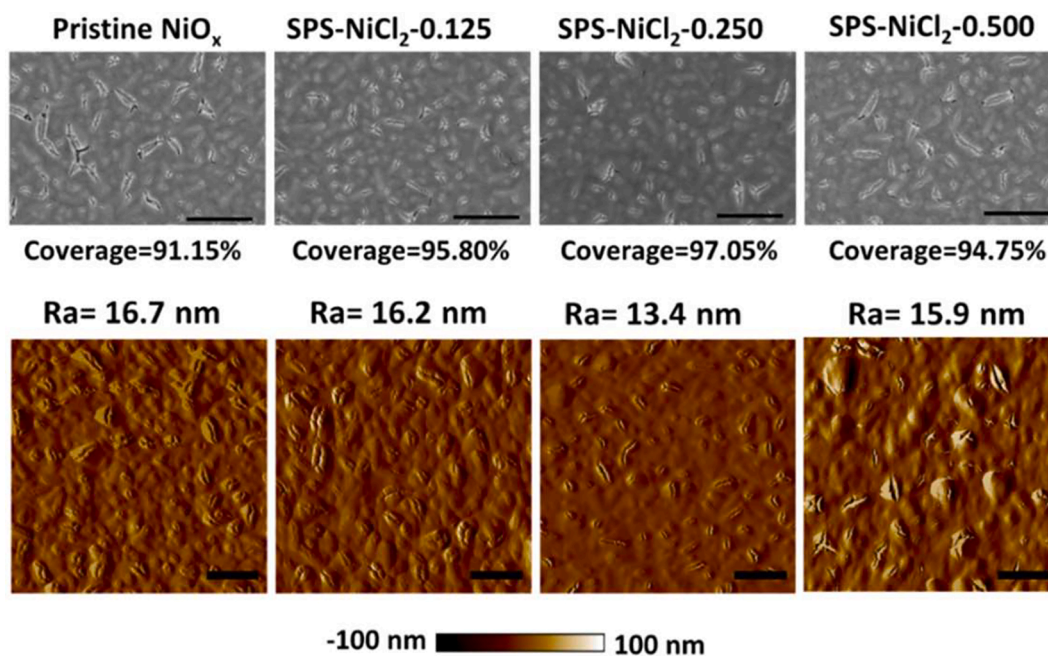


Fig. 1. Morphological characterization of NiO_x films without and with different concentrations of NiCl₂ passivation by FE-SME (first row) and topography by AFM (second row). (Scale bars indicate 1 μm).

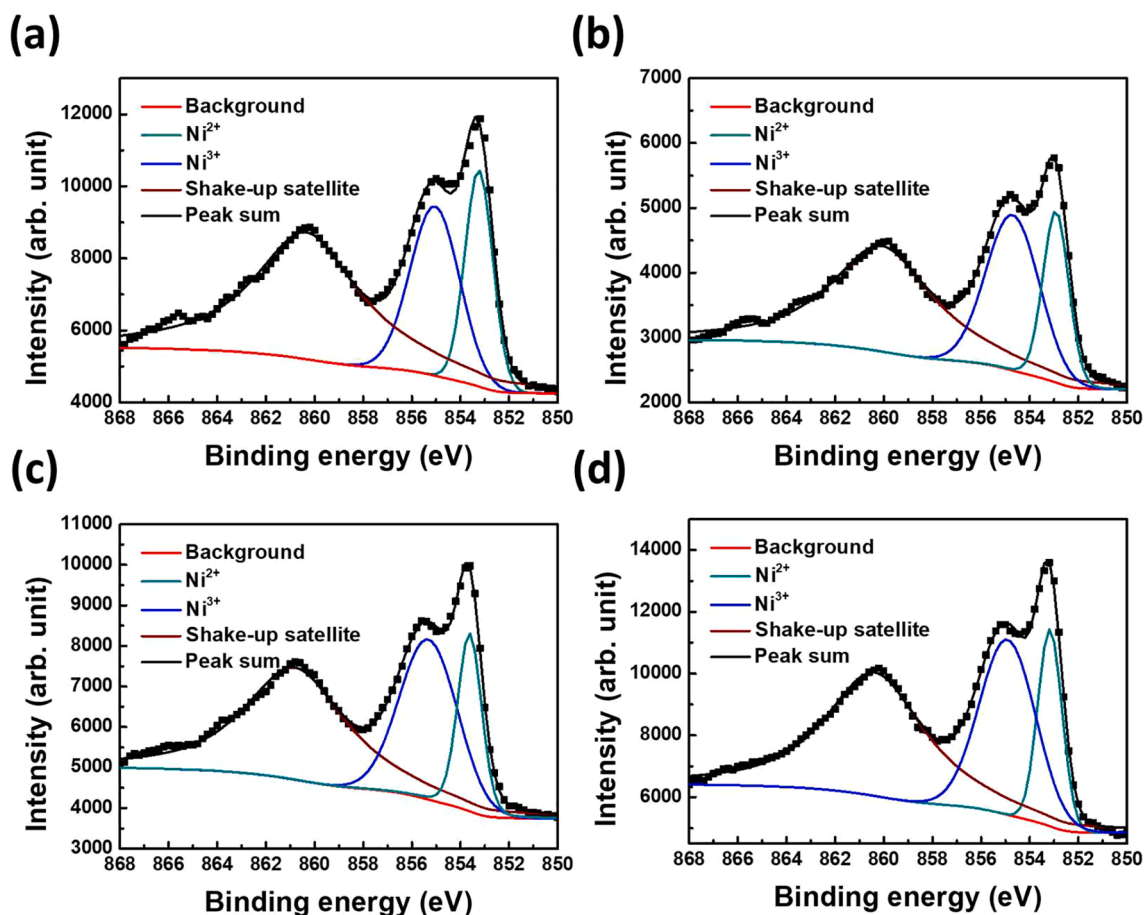


Fig. 2. Nickel oxidation state analysis of NiO_x films: (a) pristine NiO_x film, (b) SPS-NiCl₂-0.125, (c) SPS-NiCl₂-0.250, and (d) SPS-NiCl₂-0.500 treated NiO_x films.

Table 1

Chemical composition of NiO_x film and NiO_x films with different concentrations of the SPS-NiCl₂ treatment.

HTL	Ni ³⁺ /Ni (from Ni 2p) [at. %]	O/Ni [at. %]	Cl/O [at. %]
Pristine NiO _x	57.98	0.98	0
SPS-NiCl ₂ -0.125 treatment	64.59	1.08	2.27
SPS-NiCl ₂ -0.250 treatment	67.00	1.18	2.91
SPS-NiCl ₂ -0.500 treatment	67.23	1.05	3.07

Table 2

Electronic properties of NiO_x and NiO_x with different NiCl₂ concentration passivation.

HTL	Carrier density (number/cm ³)	Carrier mobility (cm ² V ⁻¹ s ⁻¹)
Pristine NiO _x	9.43×10^{14}	0.90
SPS-NiCl ₂ -0.125 treatment	1.13×10^{15}	23.30
SPS-NiCl ₂ -0.250 treatment	2.92×10^{15}	27.90
SPS-NiCl ₂ -0.500 treatment	3.38×10^{15}	13.35

be calculated by grazing-incidence wide angle X-ray scattering pattern from Figs. S4 and S5 (a). The significant improvement of carrier mobility can be attributed to the superior crystallinity of NiO_x films with the SPS-

NiCl₂ treatment as shown in Fig. S5(b). The increased grain size of NiO_x films with the SPS-NiCl₂ treatment implies a minor barrier occurs during carrier transportation. Despite the high crystallinity of the NiO_x film with 0.500 M of the SPS-NiCl₂ treatment, its detrimental surface morphology brings inflected carrier mobility. Thus, that results in a decrease in the photovoltaic performance of the corresponding OHPSCs (*vide infra*).

Besides the conductivity of NiO_x films, the energy level alignment between an HTL and a perovskite layer also determines the capability of hole extraction. The energy diagrams of OHPSCs composed of NiO_x and NiO_x with the SPS-NiCl₂ treatment were characterized by ultraviolet photoelectron spectroscopy (UPS). The energy cutoff for the work function and the energy difference between the Fermi level and VBM of NiO_x films and NiO_x films with the SPS-NiCl₂ treatment are shown in Fig. 3(a) and the full spectra are shown in Fig. S6. The UPS spectra of perovskite layer and PC₆₁BM are also shown in Fig. S7. The resulted band diagram of each layer in an OHPSC is summarized in Fig. 3(b). The large energy bandgap of HTLs allows the incident light to penetrate through effectively and to reach the absorption layer of perovskite. Also, the shallow conduction band minimum (CBM) of HTLs helps devices block electrons from perovskite layer toward anode. On the other hand, the deep energy level of valance band minimum (VBM) of PC₆₁BM also set a bar for holes from perovskite layer toward cathode. As the concentration of the SPS-NiCl₂ treatment increases, the energy level of VBM of NiO_x films shifts downward from -5.05 eV to -5.24 eV. A closed energy level between NiO_x film and perovskite layer enlarges the differences of the quasi-Fermi level at HTL/perovskite layer (E_{FP}) and perovskite layer/ETL (E_{FN}) interface. The magnitude of quasi-Fermi splitting impacts on the V_{oc} of an OHPSC. Therefore, enlarging the potential difference ($E_{FP}-E_{FN}$) is a rational way to boost the PCE of the

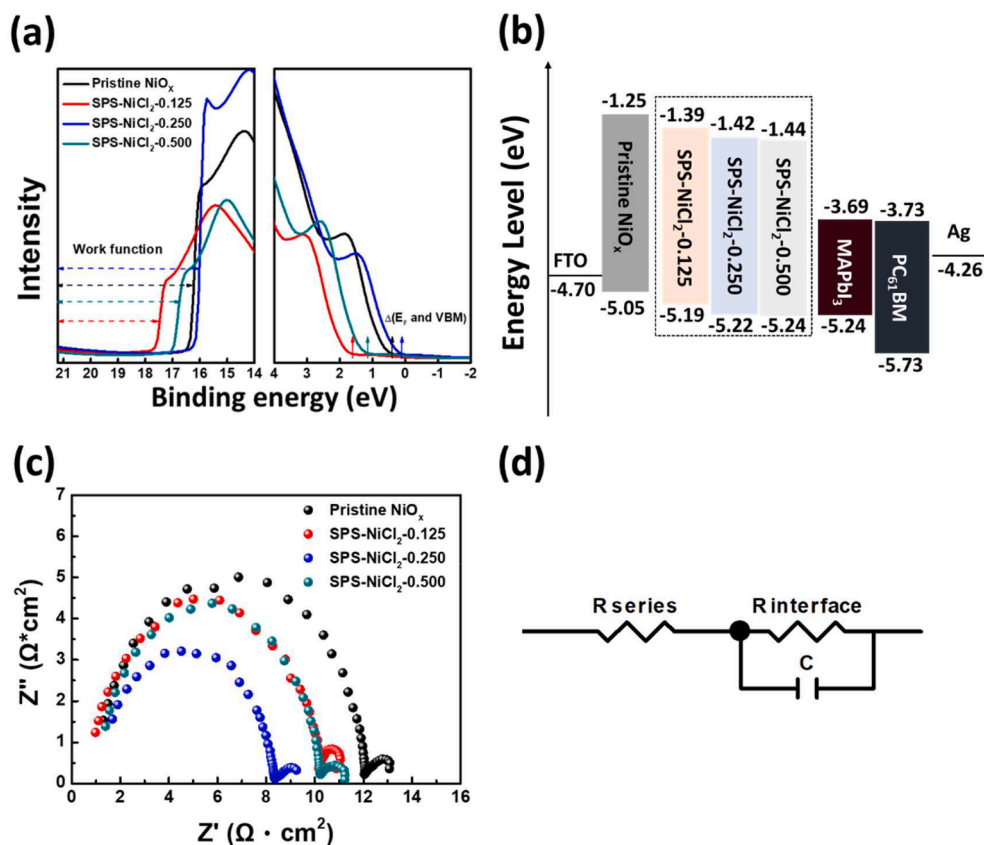


Fig. 3. Band structure characterization: (a) UPS (He I) spectrum for NiO_x and NiO_x with SPS- NiCl_2 and (b) band alignment of perovskite device with NiO_x and NiO_x with SPS- NiCl_2 ; EIS analysis of perovskite devices under $100 \text{ mW}/\text{cm}^2$ illumination: (c) typical Nyquist plot of perovskite devices with NiO_x and NiO_x with SPS- NiCl_2 and (d) equivalent circuit for model fitting.

device via enhancing its V_{oc} . In an aim to mimic a real operating condition and to investigate the interface resistance of NiO_x with and without the SPS- NiCl_2 treatment, complete devices comprised of FTO glass/ NiO_x films or NiO_x films with the SPS- NiCl_2 treatment /perovskite layer/ETL/WFL/Ag electrode were prepared to examine the electrochemical impedance and the results are shown in Fig. 3(c). The interface resistance ($R_{\text{interface}}$) of each NiO_x film can be well defined by fitting with the equivalent circuit as shown in Fig. 3(d). The $R_{\text{interface}}$ of NiO_x films was calculated as $10.92 \Omega \cdot \text{cm}^2$ for pristine NiO_x film, $9.41 \Omega \cdot \text{cm}^2$ for the sample of SPS- NiCl_2 -0.125, $7.05 \Omega \cdot \text{cm}^2$ for the sample of SPS- NiCl_2 -0.250, and $9.21 \Omega \cdot \text{cm}^2$ for sample of SPS- NiCl_2 -0.500. The highest film coverage, highest conductivity, and the suitable energy alignment contribute to the smallest $R_{\text{interface}}$ of the OHPSC that was comprised of the NiO_x film with 0.250 M of the SPS- NiCl_2 treatment.

We further measured the I - V characteristics of the OHPSCs to realize whether the aforementioned properties of the SPS- NiCl_2 treated NiO_x films were applicable to inverted OHPSCs. The results were summarized in Table S2. Without a doubt, the OHPSCs comprised of the NiO_x films with 0.250 M of the SPS- NiCl_2 treatment delivered a highest average power conversion efficiency of 17.88% with a surprising V_{oc} of 1.13 V. The reduced V_{oc} deficit encourages us to gain insight into the reason of why a tiny amount of chloride at the NiO_x /perovskite layer interface causes an obvious effect on PV performance? Therefore, OHPSCs with pristine NiO_x films were set as control devices, whereas the OHPSCs comprised of the NiO_x films with 0.250 M of the SPS- NiCl_2 treatment were set as target devices for further discussion.

To realize the spatial distribution of carrier density in control or target devices, drive-level capacitance profiling (DLCP) was measured with an alternating current (AC) at different frequencies from 1 to 1000 kHz. According to the Profiler's Equation, shown in Eq. (1) [47], a density of carriers ($\rho(W)$) and a profiling distance (W) of a junction can

be clearly described.

$$\frac{d}{dV_R} \left(\frac{1}{C^2} \right) = \frac{2}{A^2 \epsilon \epsilon_0 \rho(W)} \quad (1)$$

Here, V_R represents a reverse bias, C refers to capacitance, A implies area, $\epsilon \epsilon_0$ indicates permittivity of a material, and $\rho(W)$ is a carrier density. Based on Eq. (1), a profiling distance of W and a carrier density of $\rho(W)$ can be expressed in Eqs. (2) and (3).

$$W = \frac{\epsilon \epsilon_0 A}{C} \quad (2)$$

$$\rho(W) = \frac{2}{A^2 \epsilon \epsilon_0 \left(\frac{d}{dV_R} \left(\frac{1}{C^2} \right) \right)} \quad (3)$$

An OHPSC can be considered as a semiconductor with two junctions, which are the interfaces between perovskite layer/ETL and HTL/perovskite layer. Typically, a DLCP from a low frequency of AC is comprised of both carrier and defect density. On the contrary, applying a high-frequency AC to measure a DLCP will reveal only the concentration of free carriers. As a result, the defect density can be thoroughly depicted from DLCP as applying different frequency of AC [48,49]. The similar DLCP profiles of both control and target devices indicate that the SPS- NiCl_2 treated NiO_x film has a minor effect on carrier density of perovskite layers. The corresponding DLCPs are shown in Fig. 4(a) for a control device and Fig. 4(b) of a target device. The high carrier density at profiling distance close to origin can be referred to the ETL/perovskite layer interface, which exhibits a high carrier density. The reduction of density at profiling distance from 10 to around 550 nm implies the perovskite layers which are consistent with the thickness of perovskite layers from cross-sectional FE-SEM in Fig. S8. The climbing region of

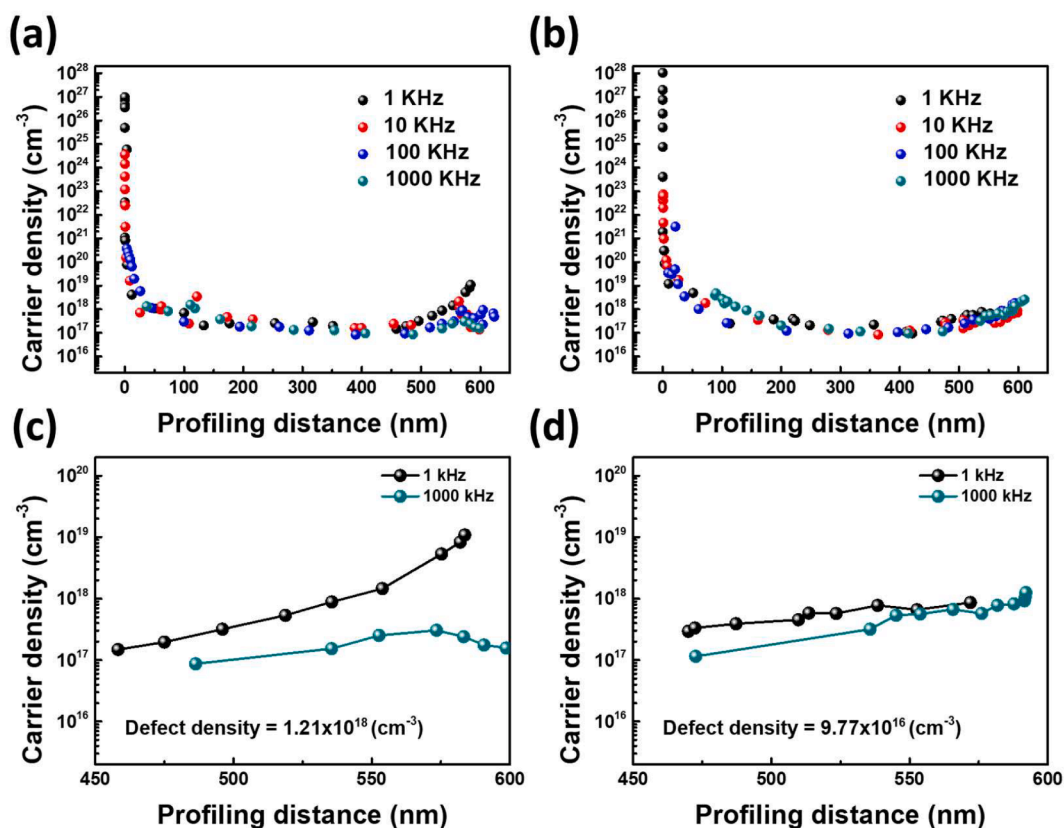


Fig. 4. Spatial carrier distribution of OHPSCs from driven-level capacitance profiling: (a) control OHPSC and (b) target OHPSC. Defect density analysis with expansion DLSP: (c) control OHPSC and (d) target OHPSC. (Distance from 450 to 600 nm).

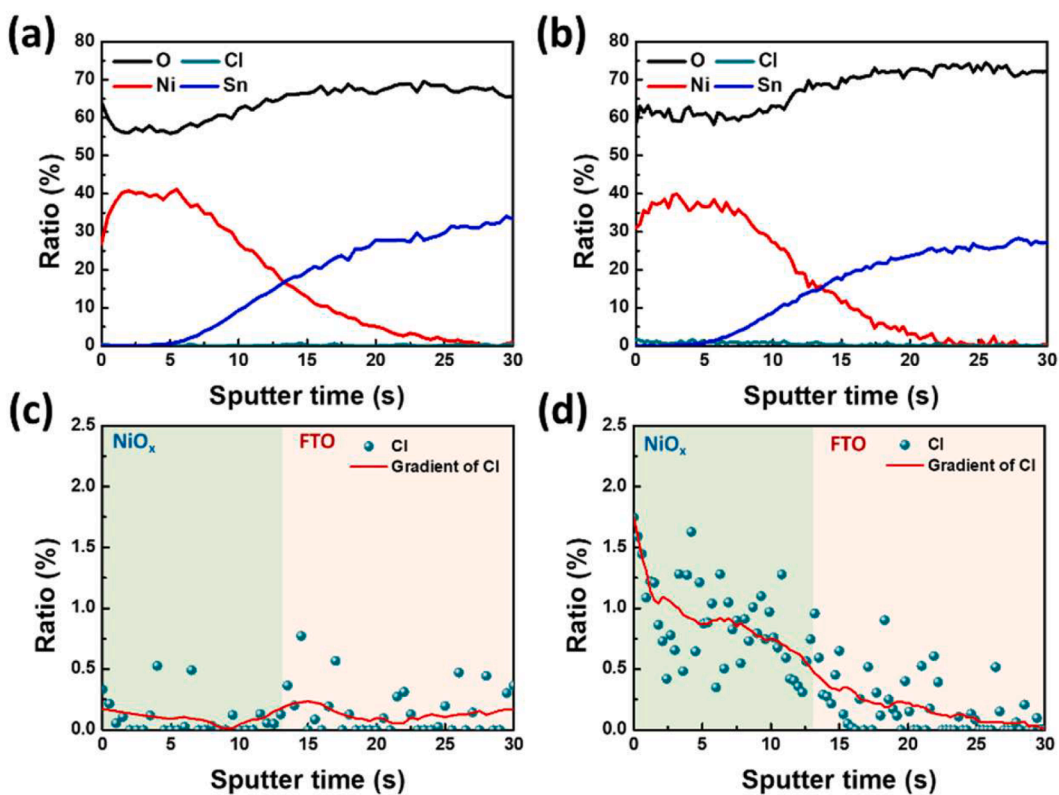


Fig. 5. XPS depth profile for the chemical composition of NiO_x film and NiO_x film with passivation: (a) pristine NiO_x, (b) SPS-NiCl₂-0.250, (c) chloride depth profile of pristine NiO_x, and (d) chloride depth profile of the SPS-NiCl₂-0.250.

carrier density at profiling distance over 500 nm can be indicative of the interface between HTL and perovskite layer. Fig. S9(a) and (b) show the DLCP with AC frequencies at 1 kHz and 1000 kHz. The defect density in HTL can be calculated by subtracting the carrier density measured at 1000 kHz from that at 1 kHz. Fig. 4(c) and (d) show the expansion DLCPs in the profiling distance from 450 nm to 600 nm. The calculated defect density of NiO_x film reduces around an order as the NiO_x film with 0.250 M of the SPS-NiCl₂ treatment.

To gain insight into the chloride distribution, depth profiles of XPS were conducted to monitor the chemical composition change of the NiO_x films without or with applying 0.250 M of the SPS-NiCl₂ treatment. Fig. 5(a) and (b) demonstrate the depth profiles of control and target device. Although a trivial concentration of chloride in the NiO_x film makes it hard to be examined from full-range spectra, the expand profiles with the ratio from 0.0 to 2.5 at. % still inform clear profiles about chloride distribution as shown in Fig. 5(c) and (d). As focusing on the chloride distributions at first 12.5 s of sputtering time, indicating the NiO_x layers, a depth depended change of chloride can be observed. Instead of distributing homogeneously, a gradient of chloride distribution was observed in the sample of SPS-NiCl₂-0.250. According to the energy diagram (Fig. 3(b)), the chloride concentration affects the energy level of NiO_x films. A clear downshift of VBM is observed as the concentration of the SPS-NiCl₂ treatment increased. Therefore, such a gradient of chloride in the sample of SPS-NiCl₂-0.250 can rationally infer that VBM gradient is created from chloride-rich HTL/perovskite layer interface of -5.22 eV to FTO/HTL interface of -5.05 eV for the target device. The chloride conferring VBM gradient not only enlarges the quasi-Fermi level splitting but also provides a convenient pathway for excited hole from perovskite layer to the anode of FTO with minor R_{interface}.

Other than the resistance analysis, the carrier transfer from OHPVSK layer to HTL can be well quantified by steady-state PL spectra and TRPL profiles. The steady-state PL spectrum in Fig. 6(a) shows the charge removal processes for perovskite film deposited either on a substrate or a substrate coated with an HTL layer. The PL intensity shows a significant quenching as the perovskite film deposited on HTL comparing to the one without HTL layer. The lowest PL intensity of perovskite film on the NiO_x film with 0.250 M of the SPS-NiCl₂ treatment reveals that the excited electron-hole pairs can be separated and transferred effectively with the assistance of VBM gradient in the SPS-NiCl₂ treated NiO_x film. On the other hand, the representative charge transfer process between the HTL and perovskite films was also investigated by TRPL spectroscopy in Fig. 6(b). The TRPL profiles were fitting with the bi-exponential model as shown in Eq. (4)

$$I(t) = A_1 \exp\left(\frac{-t}{\tau_1}\right) + A_2 \exp\left(\frac{-t}{\tau_2}\right) \quad (4)$$

Here, $I(t)$ indicates the carrier lifetime of perovskite film, τ_1 represent

the fast decay mechanism of carrier and the corresponding proportion coefficient is A_1 . In addition, τ_2 describes the slow decay behavior and its proportion coefficient is A_2 . The decay times as well as their proportional coefficient of perovskite layer with different HTL were summarized in Table 3. Based on the examined device structure with HTL, the fast decay process (τ_1) refers to the charge transfer from perovskite layer to HTL and the slow decay process (τ_2) implies the radiative decay of carriers in perovskite layer. Owing to the absence of a carrier extraction layer, the decay processes of fast and slow components for perovskite film without HTL refer to non-radiative recombination and radiative recombination, respectively. The calculated decay times for perovskite film without an HTL layer are 48.83 ns and 132.72 ns with a corresponding ratio of 53.93% and 46.07%. The weighted average decay time in the other word represents the carrier lifetime (163.28 ns) of perovskite film. For perovskite layers on pristine NiO_x film (control) and the film with 0.250 M of the SPS-NiCl₂ treatment (target), the proportion of charge transfer increase to 79.02% and 99.60%. It reveals that the charge transfer process dominates the decay process of carriers for the perovskite layer with HTL. The highest proportion coefficient as well as the shortest charge transfer time again elucidates the chloride rendering VBM gradient provides the fastest and the most effective channel for excited-holes toward HTL and anodic electrode.

The control and target OHPSCs with the structure of FTO glass / pristine NiO_x or SPS-NiCl₂-0.250/OHPVSK/PC₆₁BM/PEI/Ag were characterized to correlate the advantages of nanomorphology, interface resistance, and gradient VBM of the SPS-NiCl₂-0.250 with photovoltaic performance. Fig. 7 shows the distribution of the photovoltaic performance of 48 devices. The VBM gradient of HTLs in the target devices contributes an over 30 mV of V_{oc} enhancement as shown in Fig. 7(a). In addition, the film quality, including coverage, resistance, and non-radiative recombination improvement of the NiO_x film with 0.250 M of the SPS-NiCl₂ treatment boost the J_{sc} of target devices from average 19.66 mA/cm² to 20.96 mA/cm² as shown in Fig. 7(b). Such improvements of V_{oc} and J_{sc} of target OHPSCs, contributing from good band alignment and effective carrier transportation, directly reflect on their PCE. The average PCE for the corresponding devices increases from 16.35% to 17.88%, and the champion device reaches to 19.53% as shown in Fig. 7(e). The external quantum efficiency (EQE) of the champion devices in Fig. 7(f) is consistent with the current density

Table 3
Calculated exciton decay time and ratio of proportion coefficients of charge transfer from bi-exponential model fitting.

HTL	τ_1 (ns)	τ_2 (ns)	$A_1/(A_1+A_2)$ (%)
W/O HTL	48.83	132.72	53.93
Pristine NiO _x (Control)	16.60	52.06	79.02
SPS-NiCl ₂ -0.250 treatment (Target)	6.53	28.55	99.60

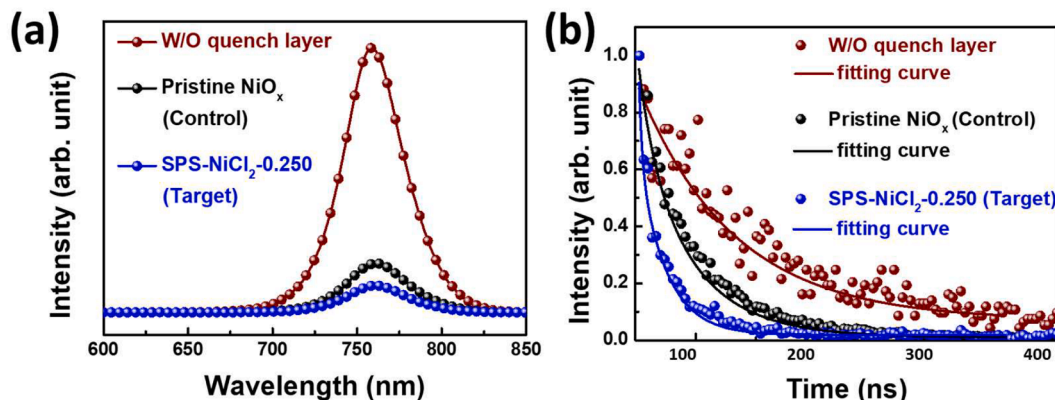


Fig. 6. Characterization of MAPbI₃ film without and with HTL: (a) PL spectrum and (b) TRPL spectrum.

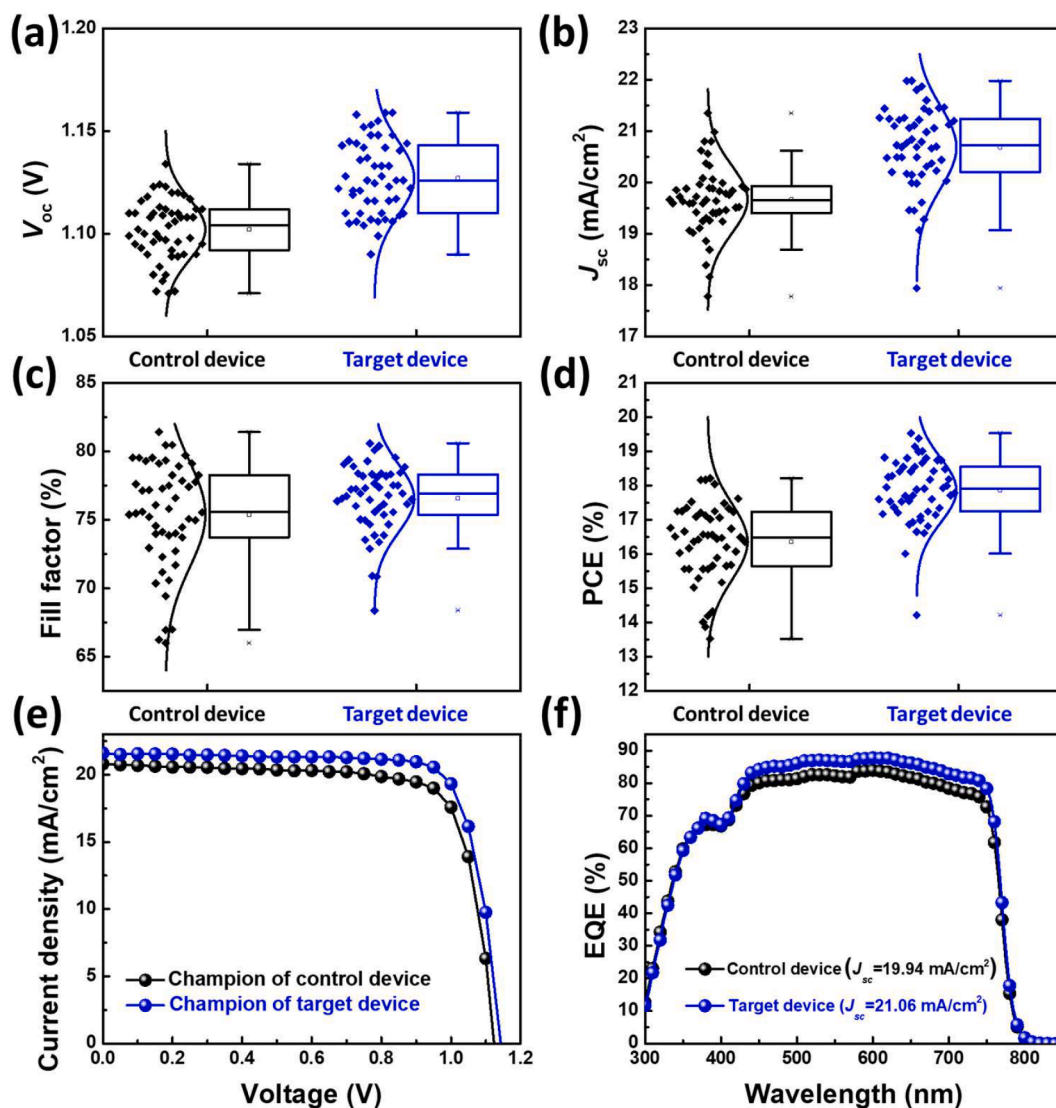


Fig. 7. Performance distribution of 48 control and target devices: (a) V_{oc} , (b) J_{sc} , (c) fill factor, and (d) PCE. Performance of champion devices: (e) $J - V$ curves and (g) EQE spectrum.

obtaining from the $I - V$ measurement.

This universal HTL with VBM gradient was also applied to the different E_g OHPSCs and showed similar results as shown in Fig. S10. The V_{oc} of the wide E_g OHPSCs can be enhanced from 1.13 V and 1.17 V for formamidium based mixed halide perovskite (CsFA based perovskite, $E_g = 1.65$ eV) and from 1.17 V to 1.23 V for methyl ammonium based mixed halide perovskite (CsMA based perovskite, $E_g = 1.70$ eV). The current density of wide bandgap OHPSCs rationally decreases owing to the narrowing absorption edge of perovskite absorber layers. However, the V_{oc} loss in a wide bandgap OHPSC is an unexpected problem and being a troublesome issue, which should be urgently resolved. By using the VBM gradient HTL, the V_{oc} loss in mixed halide perovskite solar cell can be effectively mitigated and shows the lowest V_{oc} loss in the system of NiO_x based inverted OHPSCs with the literature data as summarized into Table 4.

Fig. 8 represents the change of photovoltaic performance of encapsulated devices under damp-heat test (85 °C and 85 RH%). The stability of the target devices with the SPS- $NiCl_2$ treated NiO_x films is superior to the control devices. Although the fill factor (FF) showed unstable during the testing processes, the target devices still maintained 80% of initial PCE for 1500 h, whereas the control devices only maintained around 500 h. The suppression of interfacial effects reveals that the SPS- $NiCl_2$

treatment can improve photovoltaic performance and also offer a prospect for improving the stability of OHPSCs.

4. Conclusion

An ease of sequential passivation strategy for NiO_x film was established by using nickel chloride passivation. The SPS- $NiCl_2$ treatment confers NiO_x films to exhibit a compacted surface morphology and an energy gradient of VBM inducing from chloride gradient in depth. This universal technique of SPS- $NiCl_2$ treated NiO_x film can be directly implemented on either narrow bandgap OHPSC or wide bandgap OHPSC of methyl ammonium based or formamidium based OHPSC. The suppression of non-radiative recombination and appropriated band alignment owing to the VBM gradient mitigate the V_{oc} loss of OHPSCs for different types of active layers. The corresponding devices show V_{oc} deficits of only 470 mV for wide bandgap OHPSCs and 390 mV for narrow bandgap OHPSC. In addition to the V_{oc} loss, the VBM gradient also provides an effective path for carrier to be collected from perovskite layer to HTL and anode. Therefore, the average photovoltaic performance of device comprised of the NiO_x film with 0.250 M of the SPS- $NiCl_2$ treatment can be enhanced from 16.35% to 17.88% for narrow bandgap OHPSC, and the champion device can achieve 19.53% with

Table 4
State-of-the-art NiO_x based inverted OHPSCs with narrow and wide bandgap perovskite film.

Hole transport layer	Processing condition	Perovskite	Bandgap (eV)	V _{oc} (V)	$\frac{E_g}{q} - V_{oc}$ (mV)	J _{sc} (mA/cm ²)	FF (%)	PCE (%)	Reference
SPS-NiCl ₂ treated NiO _x	Air (RH%<10%)	MAPbI ₃	1.55	1.16	390	21.60	77.90	19.53	This work
Al:NiO _x	N ₂	MAPbI ₃	1.55	1.06	490	24.27	81.31	20.84	[50]
3D NiO _x	N ₂	MAPbI ₃	1.55	1.11	420	21.54	80.23	19.16	[51]
NiO _x NPs	N ₂	MAPbI ₃	1.55	1.07	480	–	–	19.05	[52]
S:NiO _x	N ₂	MAPbI ₃	1.55	1.10	450	23.28	80.00	20.45	[53]
Cu:NiO _x	N ₂	MAPbI ₃	1.55	1.12	430	22.14	82.00	20.21	[54]
Au embedded NiO _x	N ₂	MAPbI ₃	1.55	1.11	440	23.10	79.00	20.10	[55]
CND/urea NiO _x	N ₂	MAPbI ₃	1.55	1.06	490	23.25	79.00	19.50	[56]
NiO _x	N ₂	MAPbI ₃	1.55	1.11	440	–	–	18.84	[39]
Sr:NiO _x	N ₂	PEAI/MAPbI ₃	1.55	1.09	460	24.27	76.55	20.31	[57]
NiO _x	N ₂	MAPbI ₃	1.55	1.05	500	23.17	78.80	19.16	[58]
SPS-NiCl ₂ treated NiO _x	Air (RH%<10%)	Cs _{0.10} MA _{0.90} Pb(I _{0.8} Br _{0.2}) ₃	1.70	1.23	470	17.04	78.78	16.33	This work
SPS-NiCl ₂ treated NiO _x	Air (RH%<10%)	Cs _{0.20} FA _{0.80} Pb(I _{0.20} Br _{0.20}) ₃	1.65	1.17	480	19.44	78.44	17.76	This work
NiO _x @KCl	N ₂	Cs _{0.175} FA _{0.750} MA _{0.075} Pb(I _{0.880} Br _{0.120}) ₃	1.62	1.06	560	22.70	82.87	19.95	[59]
A-NiO _x	N ₂	(FA _{0.83} MA _{0.17}) _{0.95} Cs _{0.05} Pb(I _{0.90} Br _{0.10}) ₃	1.63	1.05	580	22.50	77.8	19.55	[60]
Cu:NiO _x	N ₂	FA _{0.85} MA _{0.15} Pb(I _{0.85} Br _{0.15}) ₃	1.65	1.14	510	22.83	81.00	21.11	[54]
NiO _x	N ₂	Cs _{0.05} FA _{0.85} MA _{0.15} Pb(I _{0.85} Br _{0.15}) ₃	1.65	1.16	490	22.88	81.40	21.63	[61]
NiO _x @KCl	N ₂	Cs _{0.05} FA _{0.85} MA _{0.15} Pb(I _{0.85} Br _{0.15}) ₃	1.65	1.15	500	22.83	79.50	20.57	[62]
NiO _x	N ₂	Cs _{0.25} FA _{0.75} Pb(Br _{0.2} I _{0.8}) ₃	1.65	1.14	510	20.34	85.00	19.66	[63]
F6TCNNQ-doped NiO _x	N ₂	Cs _{0.05} FA _{0.85} MA _{0.15} Pb(I _{0.85} Br _{0.15}) ₃	1.65	1.12	530	23.18	80.30	20.86	[64]
NiO _x	N ₂	Cs _{0.05} FA _{0.85} MA _{0.15} Pb(I _{0.85} Br _{0.15}) ₃	1.65	1.13	520	22.91	79.50	20.67	[65]

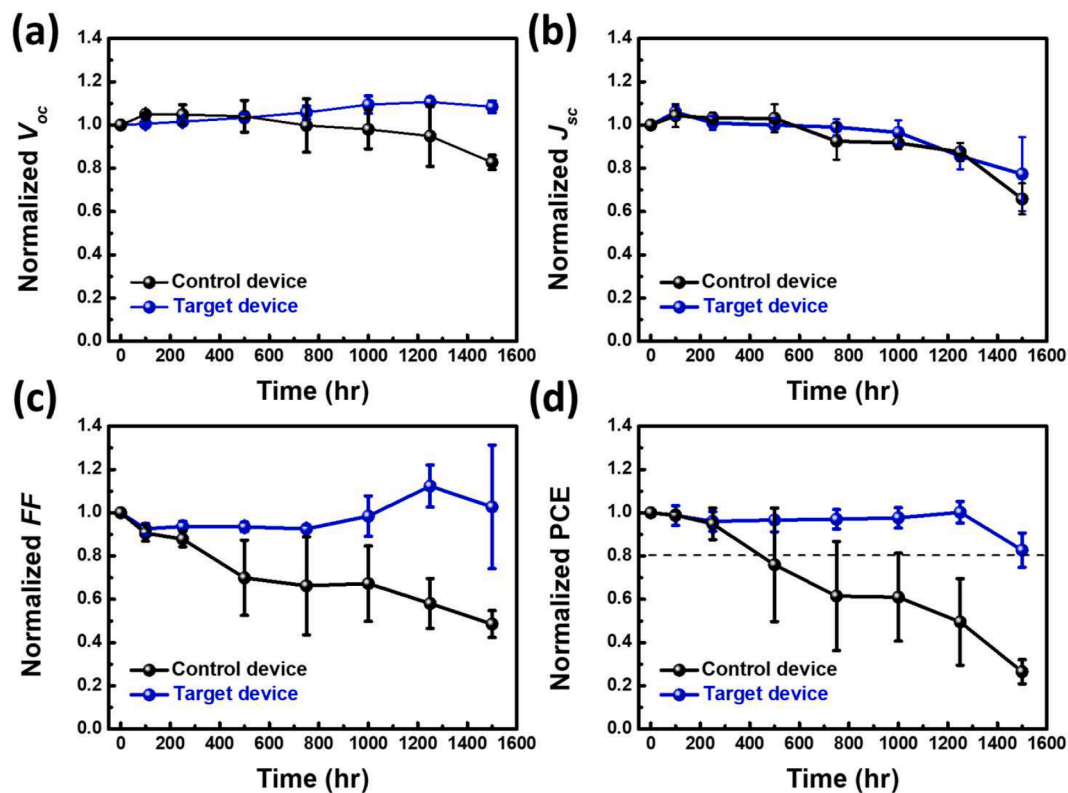


Fig. 8. Change of photovoltaic performance of encapsulated control and target devices: (a) V_{oc}, (b) J_{sc}, (c) FF, and (d) PCE. (The damp-heat tests were carried out at 85 °C and 85 RH%).

extremely high V_{oc} of 1.16 V. The damp-heat test of corresponding devices exhibit outstanding long-term stability, and over 80% of initial PCE can be maintained for 1500 h. This study provides a novel perspective for managing the interfacial issues of NiO_x in the inverted

OHPSC and opens a new avenue to develop universal HTL for perovskite layers with different E_g.

Declaration of Competing Interest

The authors declare that they have no known competing financial interests or personal relationships that could have appeared to influence the work reported in this paper.

Acknowledgments

The authors appreciate Dr. Ming-Tao Lee (BL-13A1) at National Synchrotron Radiation Research Centre for useful discussion and suggestions. This work was financially supported by the “Advanced Research Center For Green Materials Science and Technology” from The Featured Area Research Center Program within the framework of the Higher Education Sprout Project by the Ministry of Education (109L9006) and the Ministry of Science and Technology in Taiwan (MOST 108-3017-F-002-002-). The authors also thank the financial support from grant of MOST109-3116-F-002-001-CC2, and MOST 108-2119-M-002-005.

Appendix A. Supplementary data

Supplementary data to this article can be found online at <https://doi.org/10.1016/j.cej.2020.128100>.

References

- N.-G. Park, Perovskite solar cells: an emerging photovoltaic technology, *Mater. Today* 18 (2015) 65–72.
- C. La-o-vorakiat, T. Salim, J. Kadro, M.-T. Khuc, R. Haselsberger, L. Cheng, H. Xia, G.G. Gurzadyan, H. Su, Y.M. Lam, R.A. Marcus, M.-E. Michel-Beyerle, E.E.M. Chia, Elucidating the role of disorder and free-carrier recombination kinetics in CH₃NH₃PbI₃ perovskite films, *Nat. Commun.* 6 (2015) 7903.
- W. Rehman, R.L. Milot, G.E. Eperon, C. Wehrenfennig, J.L. Boland, H.J. Snaith, M. B. Johnston, L.M. Herz, Charge-carrier dynamics and mobilities in formamidinium lead mixed-halide perovskites, *Adv. Mater.* 27 (48) (2015) 7938–7944, <https://doi.org/10.1002/adma.201502969>.
- H.J. Kim, U. Kim, H.M. Kim, T.H. Kim, H.S. Mun, B.-G. Jeon, K.T. Hong, W.-J. Lee, C. Ju, K.H. Kim, K. Char, High mobility in a stable transparent perovskite oxide, *Appl. Phys. Express* 5 (2012), 061102.
- <https://www.nrel.gov/pv/cell-efficiency.html>.
- N. Marinova, W. Tress, R. Humphry-Baker, M.I. Dar, V. Bojinov, S.M. Zakeeruddin, M.K. Nazeeruddin, M. Grätzel, Light Harvesting and Charge Recombination in CH₃NH₃PbI₃ Perovskite Solar Cells Studied by Hole Transport Layer Thickness Variation, *ACS Nano* 9 (2015) 4200–4209.
- P. Schulz, Interface design for metal halide perovskite solar cells, *ACS Energy Lett.* 3 (6) (2018) 1287–1293, <https://doi.org/10.1021/acsenenergylett.8b00404>.
- T. Wang, D. Ding, H. Zheng, X. Wang, J. Wang, H. Liu, W. Shen, Efficient inverted planar perovskite solar cells using ultraviolet/ozone-treated NiOx as the hole transport layer, *Sol. RRL* 3 (2019) 1900045.
- J. Zheng, L. Hu, J.S. Yun, M. Zhang, C.F.J. Lau, J. Bing, X. Deng, Q. Ma, Y. Cho, W. Fu, C. Chen, M.A. Green, S. Huang, A.W.Y. Ho-Baillie, Solution-Processed, Silver-Doped NiOx as Hole Transporting Layer for High-Efficiency Inverted Perovskite Solar Cells, *ACS Appl. Energy Mater.* 1 (2018) 561–570.
- W. Chia-Ching, Y. Cheng-Fu, Investigation of the properties of nanostructured Li-doped NiO films using the modified spray pyrolysis method, *Nanoscale Res. Lett.* 8 (2013) 33.
- H. Lee, Y.-T. Huang, M.W. Horn, S.-P. Feng, Engineered optical and electrical performance of rf-sputtered undoped nickel oxide thin films for inverted perovskite solar cells, *Sci. Rep.* 8 (2018) 5590.
- S. Wang, B. Zhang, D. Feng, Z. Lin, J. Zhang, Y. Hao, X. Fan, J. Chang, Achieving high performance and stable inverted planar perovskite solar cells using lithium and cobalt co-doped nickel oxide as hole transport layers, *J. Mater. Chem. C* 7 (30) (2019) 9270–9277, <https://doi.org/10.1039/C9TC02526J>.
- U.K. Thakur, P. Kumar, S. Gusarov, A.E. Kobryn, S. Riddell, A. Goswami, K.M. Alam, S. Savela, P. Kar, T. Thundat, A. Meldrum, K. Shankar, Consistently High Voc Values in p-i-n Type Perovskite Solar Cells Using Ni³⁺-Doped NiO Nanomesh as the Hole Transporting Layer, *ACS Appl. Mater. Inter.* 12 (2020) 11467–11478.
- G. Niu, S. Wang, J. Li, W. Li, L. Wang, Oxygen doping in nickel oxide for highly efficient planar perovskite solar cells, *J. Mater. Chem. A* 6 (11) (2018) 4721–4728, <https://doi.org/10.1039/C8TA00161H>.
- P.-H. Lee, B.-T. Li, C.-F. Lee, Z.-H. Huang, Y.-C. Huang, W.-F. Su, High-efficiency perovskite solar cell using cobalt doped nickel oxide hole transport layer fabricated by NIR process, *Sol. Energy Mater. Sol. Cells* 208 (2020), 110352.
- M. Kim, C.W. Joo, J.H. Kim, W. Choi, J. Lee, D. Lee, H. Cho, H. Lee, S. Park, N. S. Cho, H. Cho, C.-W. Lee, D.Y. Jeon, B.-H. Kwon, Conductivity enhancement of nickel oxide by copper cation codoping for hybrid organic-inorganic light-emitting diodes, *ACS Photon.* 5 (8) (2018) 3389–3398, <https://doi.org/10.1021/acsp Photonics.8b00656.s001>.
- D.S. Kim, H.C. Lee, Nickel vacancy behavior in the electrical conductance of nonstoichiometric nickel oxide film, *J. Appl. Phys.* 112 (2012), 034504.
- H. Jin, E. Debroye, M. Keshavarz, I.G. Scheblykin, M.B.J. Roeflaers, J. Hofkens, J. A. Steele, It's a trap! On the nature of localised states and charge trapping in lead halide perovskites, *Mater. Horiz.* 7 (2) (2020) 397–410, <https://doi.org/10.1039/C9MH00500E>.
- J. Ali, Y.u. Li, P. Gao, T. Hao, J. Song, Q. Zhang, L. Zhu, J. Wang, W. Feng, H. Hu, F. Liu, Interfacial and structural modifications in perovskite solar cells, *Nanoscale* 12 (10) (2020) 5719–5745, <https://doi.org/10.1039/C9NR10788F>.
- Z. Li, Y. Tong, J. Ren, Q. Sun, Y. Tian, Y. Cui, H. Wang, Y. Hao, C.-S. Lee, Fluorinated triphenylamine-based dopant-free hole-transporting material for high-performance inverted perovskite solar cells, *Chem. Eng. J.* 402 (2020), 125923.
- B. Krogmeier, F. Staub, D. Grabowski, U. Rau, T. Kirchartz, Quantitative analysis of the transient photoluminescence of CH₃NH₃PbI₃/PC61BM heterojunctions by numerical simulations, *Sustain. Energy Fuels* 2 (2018) 1027–1034.
- W. Tress, Perovskite solar cells on the way to their radiative efficiency limit – Insights into a success story of high open-circuit voltage and low recombination, *Adv. Energy Mater.* 7 (2017) 1602358.
- U. Rau, Reciprocity relation between photovoltaic quantum efficiency and electroluminescent emission of solar cells, *Phys. Rev. B Condens. Matter* 76 (2007), 085303.
- I.L. Braly, D.W. deQuilettes, L.M. Pazos-Outón, S. Burke, M.E. Ziffer, D.S. Ginger, H.W. Hillhouse, Hybrid perovskite films approaching the radiative limit with over 90% photoluminescence quantum efficiency, *Nature Photon* 12 (6) (2018) 355–361, <https://doi.org/10.1038/s41566-018-0154-z>.
- S.S. Lim, D. Giovanni, Q. Zhang, A. Solanki, N.F. Jamaludin, J.W.M. Lim, N. Mathews, S. Mhaisalkar, M.S. Pshenichnikov, T.C. Sum, Hot carrier extraction in CH₃NH₃PbI₃ unveiled by pump-push-probe spectroscopy, *Sci. Adv.* 5 (2019) eaax3620.
- H. Tan, A. Jain, O. Voznyy, X. Lan, F.P. García de Arquer, J.Z. Fan, R. Quintero-Bermudez, M. Yuan, B.o. Zhang, Y. Zhao, F. Fan, P. Li, L.N. Quan, Y. Zhao, Z.-H. Lu, Z. Yang, S. Hoogland, E.H. Sargent, Efficient and stable solution-processed planar perovskite solar cells via contact passivation, *Science* 355 (6326) (2017) 722–726, <https://doi.org/10.1126/science.aai9081>.
- W. Gong, H. Guo, H. Zhang, J. Yang, H. Chen, L. Wang, F. Hao, X. Niu, Chlorine-doped SnO₂ hydrophobic surfaces for large grain perovskite solar cells, *J. Mater. Chem. C* 8 (2020) 11638–11646.
- H. Hu, M. Singh, X. Wan, J. Tang, C.-W. Chu, G. Li, Nucleation and crystal growth control for scalable solution-processed organic-inorganic hybrid perovskite solar cells, *J. Mater. Chem. A* 8 (4) (2020) 1578–1603, <https://doi.org/10.1039/C9TA11245F>.
- C. Bi, Q. Wang, Y. Shao, Y. Yuan, Z. Xiao, J. Huang, Non-wetting surface-driven high-aspect-ratio crystalline grain growth for efficient hybrid perovskite solar cells, *Nat. Commun.* 6 (2015) 7747.
- Y. Tu, J. Wu, X. He, P. Guo, T. Wu, H. Luo, Q. Liu, Q. Wu, J. Lin, M. Huang, Z. Lan, S. Li, A gradient engineered hole-transporting material for monolithic series-type large-area perovskite solar cells, *J. Mater. Chem. A* 5 (40) (2017) 21161–21168, <https://doi.org/10.1039/C7TA03890A>.
- T. Wu, C. Zhen, H. Zhu, J. Wu, C. Jia, L. Wang, G. Liu, N.-G. Park, H.-M. Cheng, Gradient Sn-Doped Heteroepitaxial Film of Faceted Rutile TiO₂ as an Electron Selective Layer for Efficient Perovskite Solar Cells, *ACS Appl. Mater. Inter.* 11 (2019) 19638–19646.
- W. Okada, T. Suga, K. Oyaizu, H. Segawa, H. Nishide, Perovskite/TiO₂ Interface Passivation Using Poly(vinylcarbazole) and Fullerene for the Photovoltaic Conversion Efficiency of 21%, *ACS Appl. Energy Mater.* 2 (2019) 2848–2853.
- G. Liu, H. Zheng, H. Xu, L. Zhang, X. Xu, S. Xu, X. Pan, Interface passivation treatment by halogenated low-dimensional perovskites for high-performance and stable perovskite photovoltaics, *Nano Energy* 73 (2020), 104753.
- H. Sun, D. Xie, Z. Song, C. Liang, L. Xu, X. Qu, Y. Yao, D. Li, H. Zhai, K. Zheng, C. Cui, Y. Zhao, Interface Defects Passivation and Conductivity Improvement in Planar Perovskite Solar Cells Using Na₂S-Doped Compact TiO₂ Electron Transport Layers, *ACS Appl. Mater. Inter.* 12 (2020) 22853–22861.
- J. Li, T. Bu, Z. Lin, Y. Mo, N. Chai, X. Gao, M. Ji, X.-L. Zhang, Y.-B. Cheng, F. Huang, Efficient and stable perovskite solar cells via surface passivation of an ultrathin hydrophobic organic molecular layer, *Chem. Eng. J.* 405 (2021), 126712.
- Q. Wang, C.-C. Chueh, T. Zhao, J. Cheng, M. Eslamian, W.C.H. Choy, A.-Y. Jen, Effects of Self-Assembled Monolayer Modification of Nickel Oxide Nanoparticles Layer on the Performance and Application of Inverted Perovskite Solar Cells, *ChemSusChem* 10 (19) (2017) 3794–3803, <https://doi.org/10.1002/cssc.201701262>.
- J. Zhang, H. Luo, W. Xie, X. Lin, X. Hou, J. Zhou, S. Huang, Z. Sun, X. Chen, Efficient and ultraviolet durable planar perovskite solar cells via a ferrocenecarboxylic acid modified nickel oxide hole transport layer, *Nanoscale* 10 (2018) 5617–5625.
- B. Zhang, J. Su, X. Guo, L. Zhou, Z. Lin, L. Feng, J. Zhang, J. Chang, Y. Hao, NiO/Perovskite Heterojunction Contact Engineering for Highly Efficient and Stable Perovskite Solar Cells, *Adv. Sci.* 7 (2020) 1903044.
- K.-C. Hsiao, M.-H. Jao, B.-T. Li, T.-H. Lin, S.-C. Liao, M.-C. Wu, W.-F. Su, Enhancing Efficiency and Stability of Hot Casting p-i-n Perovskite Solar Cell via Dipolar Ion Passivation, *ACS Appl. Energy Mater.* 2 (7) (2019) 4821–4832, <https://doi.org/10.1021/acsaem.9b00486.s001>.
- K.-C. Hsiao, M.-H. Jao, K.-Y. Tian, T.-H. Lin, D.-P. Tran, H.-C. Liao, C.-H. Hou, J.-J. Shyue, M.-C. Wu, W.-F. Su, Acetamidinium cation to confer ion immobilization and structure stabilization of organometal halide perovskite toward long life and high-efficiency p-i-n planar solar cell via air-processable method, *Sol. RRL* 4 (2020) 2000197.

- [41] H.-C. Liao, P. Guo, C.-P. Hsu, M. Lin, B. Wang, L. Zeng, W. Huang, C.M.M. Soe, W.-F. Su, M.J. Bedzyk, M.R. Wasielewski, A. Facchetti, R.P.H. Chang, M.G. Kanatzidis, T.J. Marks, Enhanced efficiency of hot-cast large-area planar perovskite solar cells/modules having controlled chloride incorporation, *Adv. Energy Mater.* 7 (2017) 1601660.
- [42] E.H. Anaraki, A. Kermanpur, L. Steier, K. Domanski, T. Matsui, W. Tress, M. Saliba, A. Abate, M. Grätzel, A. Hagfeldt, J.-P. Correa-Baena, Highly efficient and stable planar perovskite solar cells by solution-processed tin oxide, *Energy Environ. Sci.* 9 (10) (2016) 3128–3134, <https://doi.org/10.1039/C6EE02390H>.
- [43] D.-Y. Cho, S.J. Song, U.K. Kim, K.M. Kim, H.-K. Lee, C.S. Hwang, Spectroscopic investigation of the hole states in Ni-deficient NiO films, *J. Mater. Chem. C* 1 (28) (2013) 4334, <https://doi.org/10.1039/c3tc30687a>.
- [44] S. Kim, J.S. Kang, S. Kim, S. Kang, Y.-E. Sung, K. Cho, J. Yoon, Electrochemical regeneration of free chlorine treated nickel oxide catalysts for oxidation of aqueous pollutants, *Catalysis Today* (2020), <https://doi.org/10.1016/j.cattod.2020.03.045>.
- [45] D. Adler, J. Feinleib, Electrical and optical properties of narrow-band materials, *Phys. Rev. B* 2 (8) (1970) 3112–3134, <https://doi.org/10.1103/PhysRevB.2.3112>.
- [46] P. Dubey, N. Kaurav, R.S. Devan, G.S. Okram, Y.K. Kuo, The effect of stoichiometry on the structural, thermal and electronic properties of thermally decomposed nickel oxide, *RSC Adv.* 8 (11) (2018) 5882–5890, <https://doi.org/10.1039/C8RA00157J>.
- [47] N.D. Reynolds, C.D. Panda, J.M. Essick, Capacitance-voltage profiling: Research-grade approach versus low-cost alternatives, *Am. J. Phys.* 82 (2014) 196–205.
- [48] Z. Ni, C. Bao, Y.e. Liu, Q.i. Jiang, W.-Q. Wu, S. Chen, X. Dai, B.o. Chen, B. Hartweg, Z. Yu, Z. Holman, J. Huang, Resolving spatial and energetic distributions of trap states in metal halide perovskite solar cells, *Science* 367 (6484) (2020) 1352–1358, <https://doi.org/10.1126/science.aba0893>.
- [49] W.-Q. Wu, P.N. Rudd, Z. Ni, C.H. Van Brackle, H. Wei, Q.i. Wang, B.R. Ecker, Y. Gao, J. Huang, Reducing surface halide deficiency for efficient and stable iodide-based perovskite solar cells, *J. Am. Chem. Soc.* 142 (8) (2020) 3989–3996, <https://doi.org/10.1021/jacs.9b13418.s001>.
- [50] B. Parida, S. Yoon, J. Ryu, S. Hayase, S.M. Jeong, D.-W. Kang, Boosting the Conversion Efficiency Over 20% in MAPbI₃ Perovskite Planar Solar Cells by Employing a Solution-Processed Aluminum-Doped Nickel Oxide Hole Collector, *ACS Appl. Mater. Inter.* 12 (2020) 22958–22970.
- [51] X. Yin, J. Zhai, P. Du, N.i. Li, L. Song, J. Xiong, F. Ko, 3 D NiO Nanowall Hole-Transporting Layer for the Passivation of Interfacial Contact in Inverted Perovskite Solar Cells, *ChemSusChem* 13 (5) (2020) 1006–1012, <https://doi.org/10.1002/cssc.201903025>.
- [52] S. Maddala, C.-L. Chung, S.-Y. Wang, K. Kollimalayan, H.-L. Hsu, P. Venkatakrishnan, C.-P. Chen, Y.J. Chang, Forming a metal-free oxidatively coupled agent, bicarbazole, as a defect passivation for htm and an interfacial layer in a p-i-n perovskite solar cell exhibits nearly 20% efficiency, *Chem. Mater.* 32 (1) (2020) 127–138, <https://doi.org/10.1021/acs.chemmater.9b02720.s001>.
- [53] C. Hu, Y. Bai, S. Xiao, K. Tao, W.K. Ng, K.S. Wong, S.H. Cheung, S.K. So, Q. Chen, S. Yang, Surface Sulfuration of NiO Boosts the Performance of Inverted Perovskite Solar Cells, *Sol. RRL* 4 (2020) 2000270.
- [54] K. Yao, S. Leng, Z. Liu, L. Fei, Y. Chen, S. Li, N. Zhou, J. Zhang, Y.-X. Xu, L. Zhou, H. Huang, A.-Y. Jen, Fullerene-anchored core-shell ZnO nanoparticles for efficient and stable dual-sensitized perovskite solar cells, *Joule* 3 (2) (2019) 417–431, <https://doi.org/10.1016/j.joule.2018.10.018>.
- [55] S. Xiao, F. Xu, Y. Bai, J. Xiao, T. Zhang, C. Hu, X. Meng, H. Tan, H.-P. Ho, S. Yang, An ultra-low concentration of gold nanoparticles embedded in the NiO hole transport layer boosts the performance of p-i-n perovskite solar cells, *Sol. RRL* 3 (2019) 1800278.
- [56] H.-L. Hsu, H.-T. Hsiao, T.-Y. Juang, B.-H. Jiang, S.-C. Chen, R.-J. Jeng, C.-P. Chen, Carbon nanodot additives realize high-performance air-stable p-i-n perovskite solar cells providing efficiencies of up to 20.2%, *Adv. Energy Mater.* 8 (2018) 1802323.
- [57] Y. Liu, J. Duan, J. Zhang, S. Huang, W. Ou-Yang, Q. Bao, Z. Sun, X. Chen, High Efficiency and Stability of Inverted Perovskite Solar Cells Using Phenethyl Ammonium Iodide-Modified Interface of NiOx and Perovskite Layers, *ACS Appl. Mater. Inter.* 12 (2020) 771–779.
- [58] X. Zheng, Z. Song, Z. Chen, S.S. Bista, P. Gui, N. Shrestha, C. Chen, C. Li, X. Yin, R. A. Awni, H. Lei, C. Tao, R.J. Ellingson, Y. Yan, G. Fang, Interface modification of sputtered NiOx as the hole-transporting layer for efficient inverted planar perovskite solar cells, *J. Mater. Chem. C* 8 (2020) 1972–1980.
- [59] P. Patil, D.S. Mann, U.T. Nakate, Y.-B. Hahn, S.-N. Kwon, S.-I. Na, Hybrid interfacial ETL engineering using PCBM-SnS₂ for high-performance p-i-n structured planar perovskite solar cells, *Chem. Eng. J.* 397 (2020), 125504.
- [60] Z. Wang, X. Rong, L. Wang, W. Wang, H. Lin, X. Li, Dual Role of Amino-Functionalized Graphene Quantum Dots in NiOx Films for Efficient Inverted Flexible Perovskite Solar Cells, *ACS Appl. Mater. Inter.* 12 (2020) 8342–8350.
- [61] W. Chen, G. Pang, Y. Zhou, Y. Sun, F.-Z. Liu, R. Chen, S. Chen, A.B. Djurišić, Z. He, Stabilizing n-type hetero-junctions for NiOx based inverted planar perovskite solar cells with an efficiency of 21.6%, *J. Mater. Chem. A* 8 (2020) 1865–1874.
- [62] W. Chen, Y. Zhou, G. Chen, Y. Wu, B. Tu, F.-Z. Liu, L. Huang, A.M.C. Ng, A. B. Djurišić, Z. He, Alkali chlorides for the suppression of the interfacial recombination in inverted planar perovskite solar cells, *Adv. Energy Mater.* 9 (2019) 1803872.
- [63] C.C. Boyd, R.C. Shallcross, T. Moot, R. Kerner, L. Bertoluzzi, A. Onno, S. Kavadiya, C. Chosy, E.J. Wolf, J. Werner, J.A. Raiford, C. de Paula, A.F. Palmstrom, Z.J. Yu, J. J. Berry, S.F. Bent, Z.C. Holman, J.M. Luther, E.L. Ratcliff, N.R. Armstrong, M. D. McGehee, Overcoming redox reactions at perovskite-nickel oxide interfaces to boost voltages in perovskite solar cells, *Joule* 4 (8) (2020) 1759–1775, <https://doi.org/10.1016/j.joule.2020.06.004>.
- [64] W. Chen, Y. Zhou, L. Wang, Y. Wu, B. Tu, B. Yu, F. Liu, H.-W. Tam, G. Wang, A. B. Djurišić, L. Huang, Z. He, Molecule-doped nickel oxide: verified charge transfer and planar inverted mixed cation perovskite solar cell, *Adv. Mater.* 30 (2018) 1800515.
- [65] W. Chen, Y. Wang, G. Pang, C.W. Koh, A.B. Djurišić, Y. Wu, B. Tu, F.-Z. Liu, R. Chen, H.Y. Woo, X. Guo, Z. He, Conjugated polymer-assisted grain boundary passivation for efficient inverted planar perovskite solar cells, *Adv. Funct. Mater.* 29 (2019) 1808855.